nature geoscience

SUPPLEMENTARY INFORMATION

https://doi.org/10.1038/s41561-019-0347-1

In the format provided by the authors and unedited.

Seismic velocity reduction and accelerated recovery due to earthquakes on the Longmenshan fault

Shunping Pei[1,2], Fenglin Niu[3,4]*, Yehuda Ben-Zion[5], Quan Sun[2], Yanbing Liu[2], Xiaotian Xue[2], Jinrong Su[6] and Zhigang Shao[7]

[1]CAS Center for Excellence in Tibetan Plateau Earth Sciences, Chinese Academy of Sciences (CAS), Beijing, China. [2]CAS Key Laboratory of Continental Collision and Plateau Uplift, Institute of Tibetan Plateau Research, Chinese Academy of Sciences (CAS), Beijing, China. [3]State Key Laboratory of Petroleum Resources and Prospecting, and Unconventional Gas Institute, China University of Petroleum at Beijing, Beijing, China. [4]Department of Earth, Environmental and Planetary Sciences, Rice University, Houston, TX, USA. [5]Department of Earth Sciences, University of Southern California, Los Angeles, CA, USA. [6]Earthquake Administration of Sichuan Province, Chengdu, China. [7]Institute of Earthquake Science, China Earthquake Administration, Beijing, China. *e-mail: niu@rice.edu

Seismic velocity reduction and accelerated recovery due to earthquakes on the Longmenshan fault

Supplementary Information

Shunping Pei[1,2], Fenglin Niu[3,4], Yehuda Ben-Zion[5], Quan Sun[2], Yanbing Liu[2], Xiaotian Xue[2], Jinrong Su[6], Zhigang Shao[7]

[1]*CAS Centre for Excellence in Tibetan Plateau Earth Sciences, Chinese Academy of Sciences (CAS), Beijing 100101, China.*

[2] *CAS Key Laboratory of Continental Collision and Plateau Uplift, Institute of Tibetan Plateau Research, Chinese Academy of Sciences, Beijing 100101, China*

[3]*State Key Laboratory of petroleum Resource and Prospecting, and Unconventional Gas Institute, China University of Petroleum at Beijing, Beijing 102249, China*

[4]*Department of Earth, Environmental and Planetary Sciences, Rice University, 6100 Main Street, Houston, TX 77005, USA*

[5]*Department of Earth Sciences, University of Southern California, Los Angeles, CA 90089, USA*

[6]*Earthquake Administration of Sichuan Province, Chengdu 610041, China*

[7]*Institute of Earthquake Science, China Earthquake Administration, Beijing 100029, China*

S1. Data Selection and Inversions

We selected the Pg-wave traveltime data in the distance of 0.1°-2.0° recorded by the regional seismic network operated by the Earthquake Administration of Sichuan Province in the period between 2000 and 2014. Since Pg is the first arrival with relatively high frequency (5-20 Hz), it can be easily picked with an uncertainty less than 0.1 s. To invert for the coseismic and postseismic seismic velocity changes of the Wenchuan earthquake (WCEQ) and Lushan earthquake (LSEQ) along the Longmenshan fault, we selected four periods, which have roughly the similar amount of raypaths (Table S1). As shown in Figure S1, the Pg travel times exhibit a well-defined linear trend in the selected distance range. The average P-wave velocity can be obtained from the slope of the linear trend. To investigate the temporal changes of the average P-wave velocity, we used a one-year and a one-month or two-month interval before and after the Wenchuan earthquake, respectively. The numbers of seismic stations, earthquakes, and raypaths as well as the calculated the average P-wave velocity and one-sigma standard deviation of each period are listed in Table S2.

For the 2-D tomographic inversion, the travel time data were divided into four periods (P1, P2, P3, and P4). In all the four periods, the Longmenshan fault zone was well sampled by the selected Pg rays (Figure S2). We discretized the study area with 0.05º×0.05º cells, and most of the cells along the Longmenshan fault are well sampled by a few hundreds to a thousand Pg rays (Figure S3).

Table S1. Data of the four periods

Period	Time Window	No. Stations	No. Events	No. Raypaths	Distance§ (km)	Depth¶ (km)
P1 (before WCEQ)	2000.01 - 2008.04	27	1498	11814	108.2±52.8	6.9±4.5
P2 (after WCEQ)	2008.05 - 2008.07	34	2095	14846	92.8±47.9	9.3±7.6
P3 (before LSEQ)	2011.07 - 2012.12	31	1864	17746	85.7±46.5	11.7±4.5
P4 (after LSEQ)	2013.05 - 2014.09	50	1739	19003	82.5±48.4	13.5±4.7

§: Average epicentre distance and one-sigma standard deviation; ¶: average focal depth and one-sigma standard deviation.

Table S2. The average velocities with error in Figure 2 for WCEQ and LSEQ area.

Year	Month	No. Stations	No. Events	No. Raypaths	Vp (km/s)	Error (km/s)
2001		21	164	1201	6.013	0.020
2002		21	205	1538	5.995	0.017
2003		20	219	1565	6.043	0.018
2004		20	210	1608	5.996	0.016
2005		20	143	1288	6.012	0.017
2006		23	173	1565	5.957	0.014
2007		23	201	1728	6.034	0.014
2008	5	22	1033	6032	5.772	0.004
2008	6	22	778	5646	5.762	0.004
2008	7	34	735	6522	5.755	0.004
2008	8	37	1560	14786	5.746	0.003
2008	9	45	1071	13800	5.749	0.003
2008	10	45	869	10990	5.757	0.003
2008	11	48	747	9793	5.755	0.003
2008	12	39	626	7621	5.741	0.004
2009	1	39	572	6364	5.754	0.004
2009	2	39	470	5555	5.751	0.004
2009	3	39	500	5832	5.745	0.004
2009	4	42	436	5108	5.785	0.005
2009	5	41	398	4475	5.774	0.005
2009	6	38	383	4372	5.786	0.005
2009	7	36	333	3736	5.776	0.005
2009	8	37	285	3363	5.759	0.006
2009	9	36	274	3229	5.784	0.005
2009	10	36	248	2891	5.753	0.006
2009	11	34	243	2701	5.735	0.006

2009	12	36	239	2632	5.759	0.006
2010	1	31	200	2100	5.746	0.007
2010	2	34	175	2133	5.806	0.007
2010	3	35	236	2709	5.779	0.006
2010	4	34	181	2161	5.769	0.007
2010	5	34	220	2582	5.808	0.007
2010	6	34	190	2158	5.799	0.007
2010	7	35	226	2552	5.803	0.007
2010	8	31	181	1973	5.834	0.008
2010	9	30	163	1706	5.805	0.008
2010	10	33	170	1697	5.793	0.008
2010	11	28	158	1474	5.817	0.008
2010	12	25	146	1177	5.846	0.010
2011	1	26	162	1501	5.822	0.008
2011	2	26	142	1460	5.816	0.008
2011	3	27	148	1339	5.795	0.009
2011	4	27	149	1399	5.807	0.009
2011	5	27	110	1002	5.783	0.010
2011	6	27	123	1108	5.785	0.010
2011	7	24	113	987	5.777	0.010
2011	8	27	105	876	5.814	0.011
2011	9	26	106	886	5.832	0.011
2011	10	27	100	806	5.843	0.012
2011	11	28	113	885	5.860	0.011
2011	12	28	96	772	5.852	0.012
2012	1	22	146	1281	5.907	0.010
2012	3	27	200	1815	5.814	0.008
2012	5	27	230	2251	5.844	0.007
2012	7	28	211	1953	5.787	0.008
2012	9	28	219	2109	5.831	0.008
2012	11	28	175	1694	5.806	0.008
2013	1	34	180	1977	5.832	0.008
2013	3	50	916	8317	5.725	0.004
2013	5	47	354	4588	5.895	0.004
2013	7	27	227	1971	5.899	0.007
2013	9	27	187	1568	5.886	0.008
2013	11	26	156	1322	5.890	0.008
2014	1	26	128	1325	5.917	0.008
2014	3	26	154	1394	5.897	0.008
2014	5	27	137	1165	5.893	0.008
2014	7	27	130	1137	5.979	0.010
2014	9	28	156	1553	5.907	0.008
2000.01-2008.04*		8	410	1705	6.016	0.048
2008.05-2013.03*		10	285	1491	6.046	0.044
2013.04-2014.12*		22	1126	8057	5.763	0.009

*Here for travel time data in LSEQ area (black dashed square in Figure 1b) and the others for WCEQ area (blue dashed square in Figure 1a).

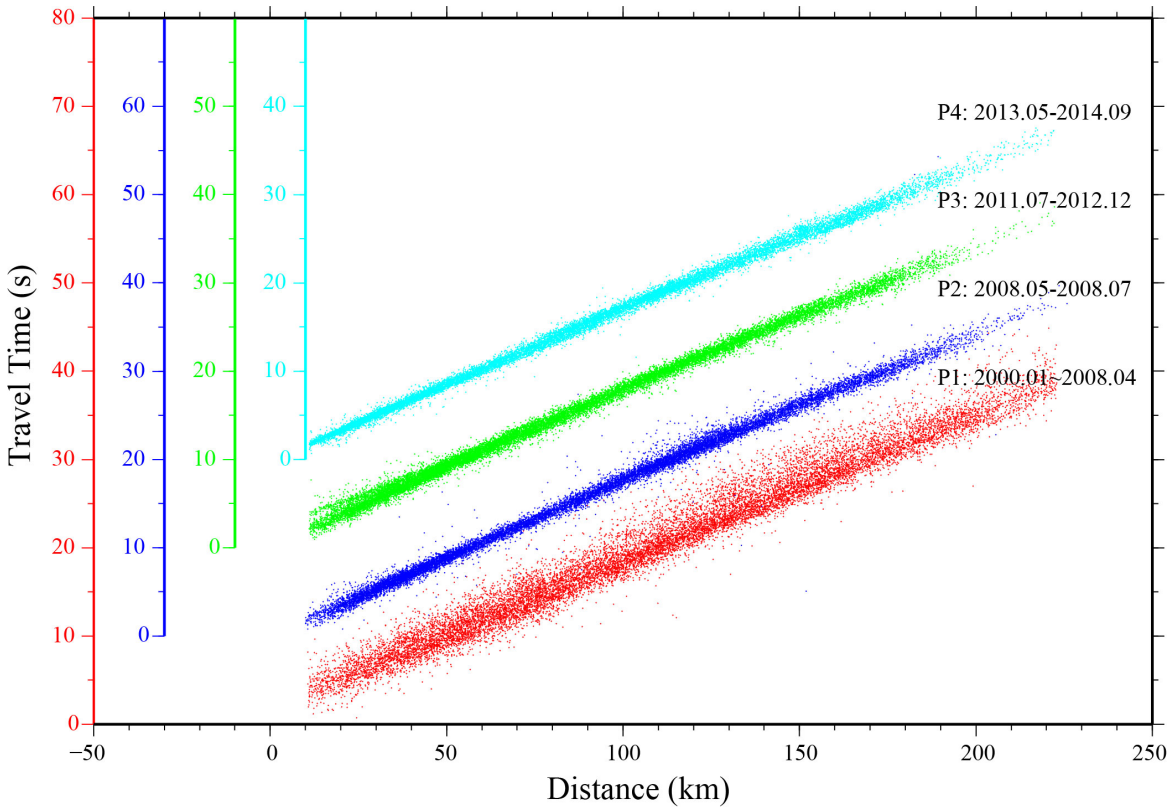

Figure S1. Pg traveltimes of the four periods picked from the local seismic network. The four periods are: P1, 2000.01-2008.04; P2, 2008.05-2008.07; P3, 2011.07~2012.12; P4, 2013.05~2014.09. Traveltime data with residuals <2.0 s are used in inverting spatial and temporal variations of the upper crustal velocity structure around the Longmenshan fault zone.

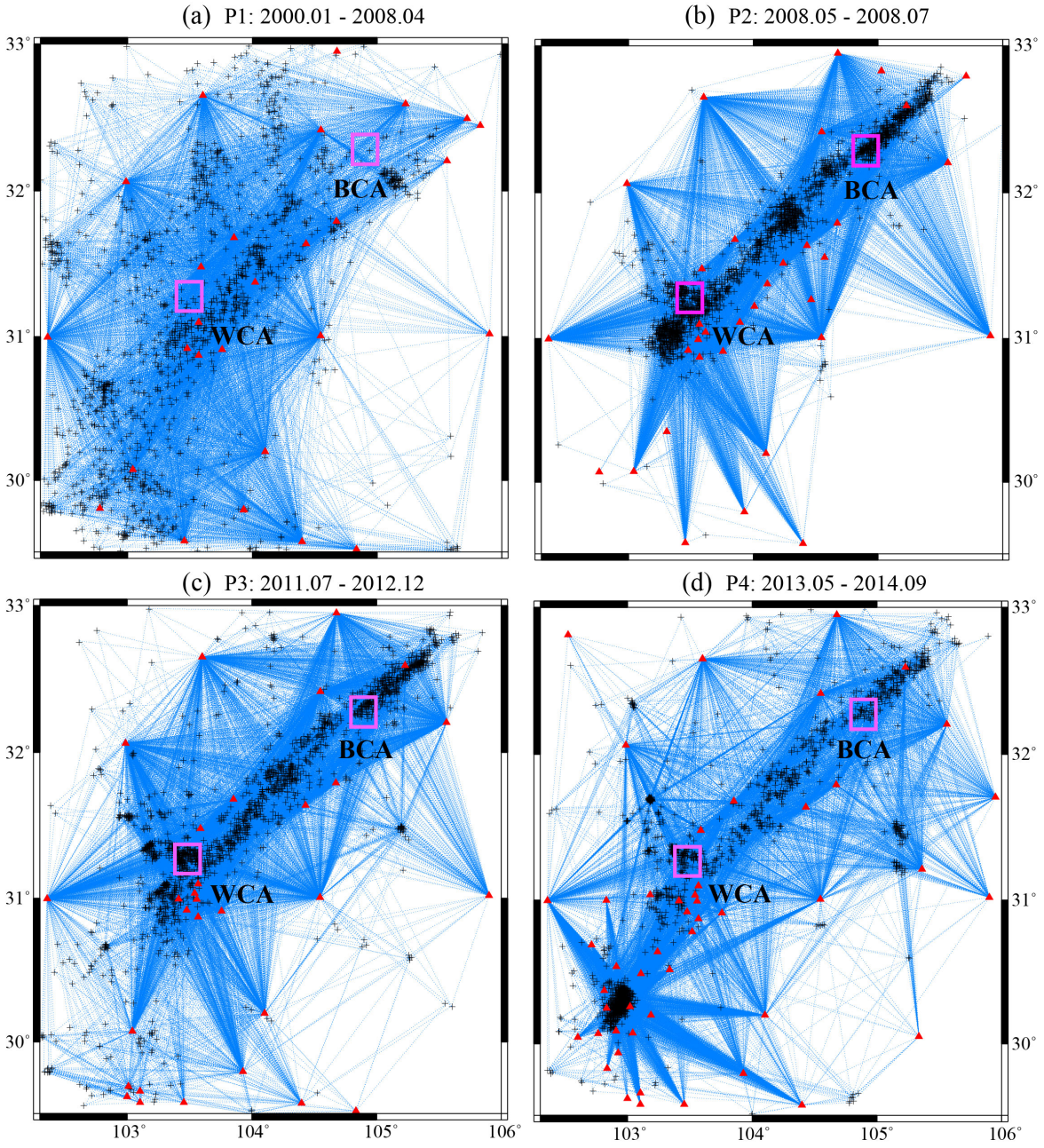

Figure S2. Raypath coverage of each period with crosses and triangles representing the earthquakes and stations, respectively. The pink squares show the Wenchuan asperity (WCA) and Beichuan asperity (BCA), respectively.

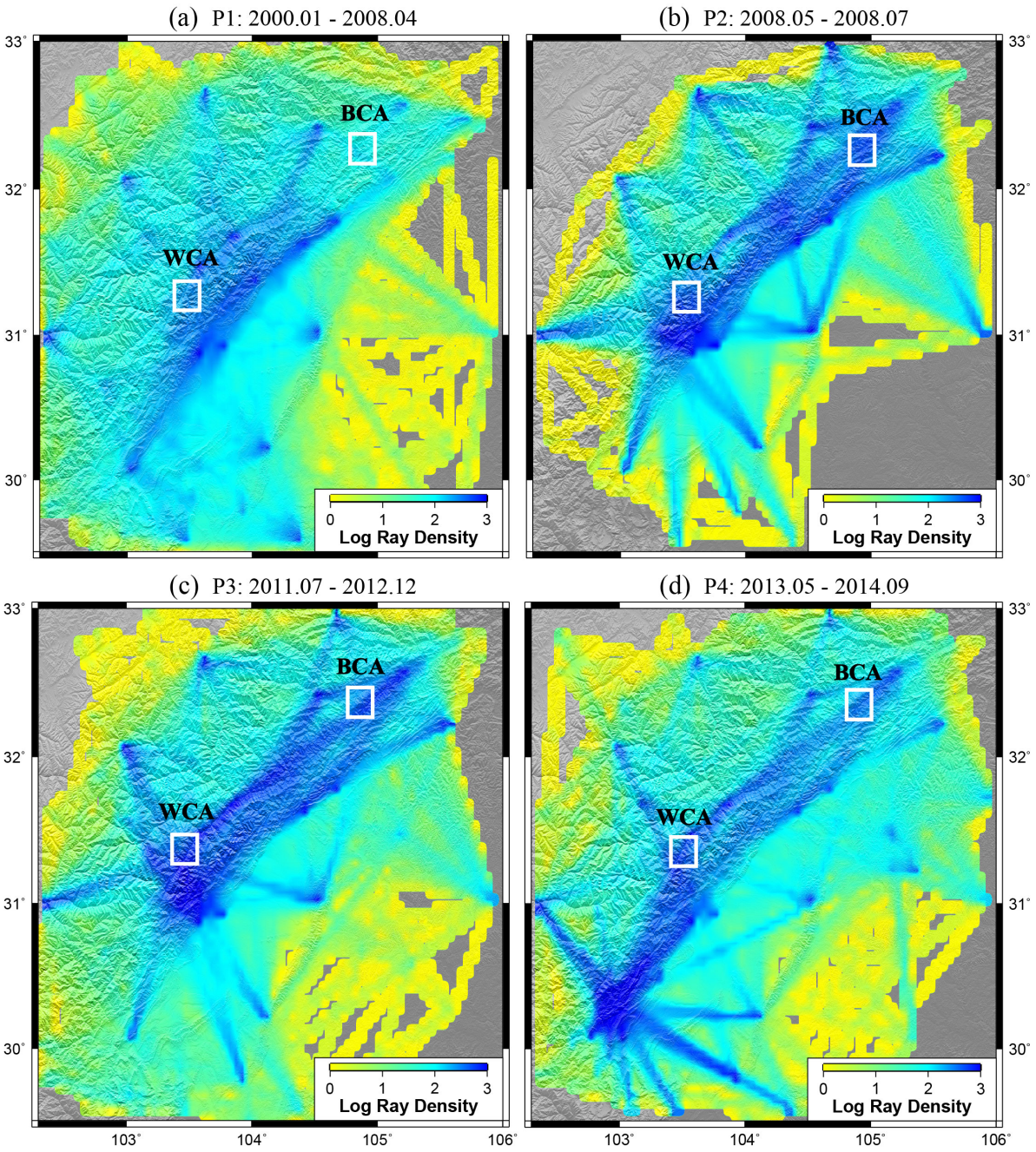

Figure S3. Maps showing the density of raypath coverage of the four periods. The color represents the hit counts of ray path at each cell with size of 3 by 3 minutes. The number of color scale indicates logarithm of the hit counts. The densest ray coverage occurred in Longmenshan fault zone at all four periods.

S2. Smoothing and damping parameters

We employed a smoothing parameter λ_1 and a damping parameter λ_2 to regularize the spatial (δs) and temporal (Δs) variations of the slowness field, respectively. As we expect that temporal velocity changes outside the Longmenshan fault zone is likely insignificant, therefore we set the damping parameter away

from the Longmenshan fault zone (cells out of the white box in Figure 1b) four times larger than that in the box (λ_2). We employed four different λ_1, 200, 300, 500, and 1000, as well as four different λ_2, 10, 50, 100, and 200, so we conducted a total of 16 joint inversions for the selected two periods. The resulting temporal variations are shown in Figure S4. After a series of tests, we found that (λ_1, λ_2) =(500,50) seems to lead to results with good resolution and stability.

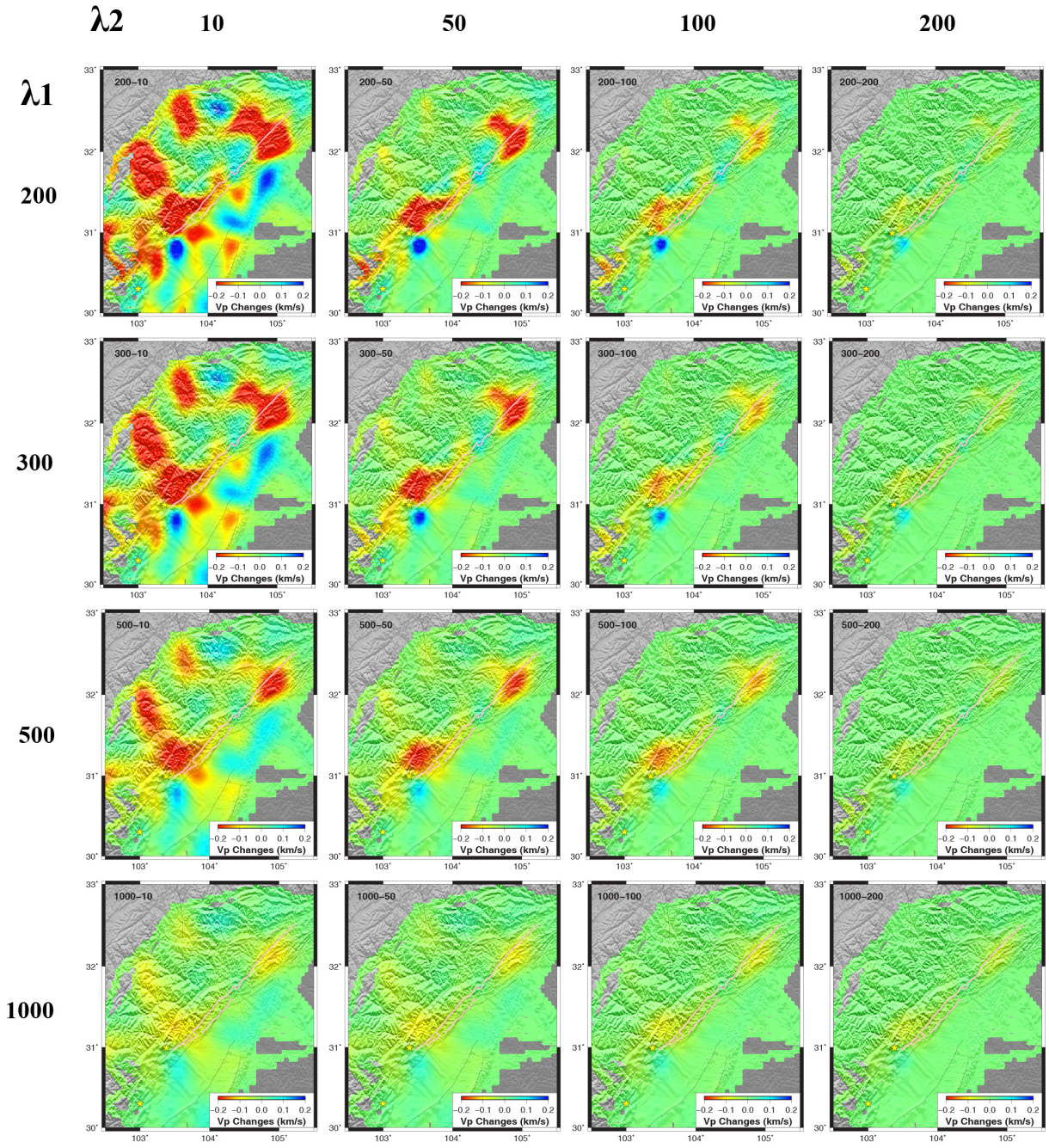

Figure S4. Inverted coseismic velocity changes of the WCEQ (difference between P2 and P1) are shown as a function of smoothing (λ_1, vertical axis) and damping (λ_2, horizontal axis) parameters.

S3. Resolution tests

We conducted checkerboard tests to evaluate the spatial resolution of the selected Pg raypath coverage. We created a test checkerboard velocity model by adding sinusoidal velocity perturbations with amplitude of 0.4 km/s to a uniform velocity model with a velocity of 6 km/s. We then computed the travel times using the checkerboard model for all the Pg raypaths used in the real data inversion. We also added Gaussian noise with standard deviation 0.1 s, based on the uncertainty in picking the Pg arrival time to synthetic travel time dataset. Finally we inverted the synthetic travel time dataset for velocity variations in a similar way that we inverted the real data. The inverted velocity perturbations from a 0.25º×0.25º checkerboard model are shown in Figure S5. We found that our Pg data have a lateral resolution of 0.25º×0.25º within the Longmenshan fault zone.

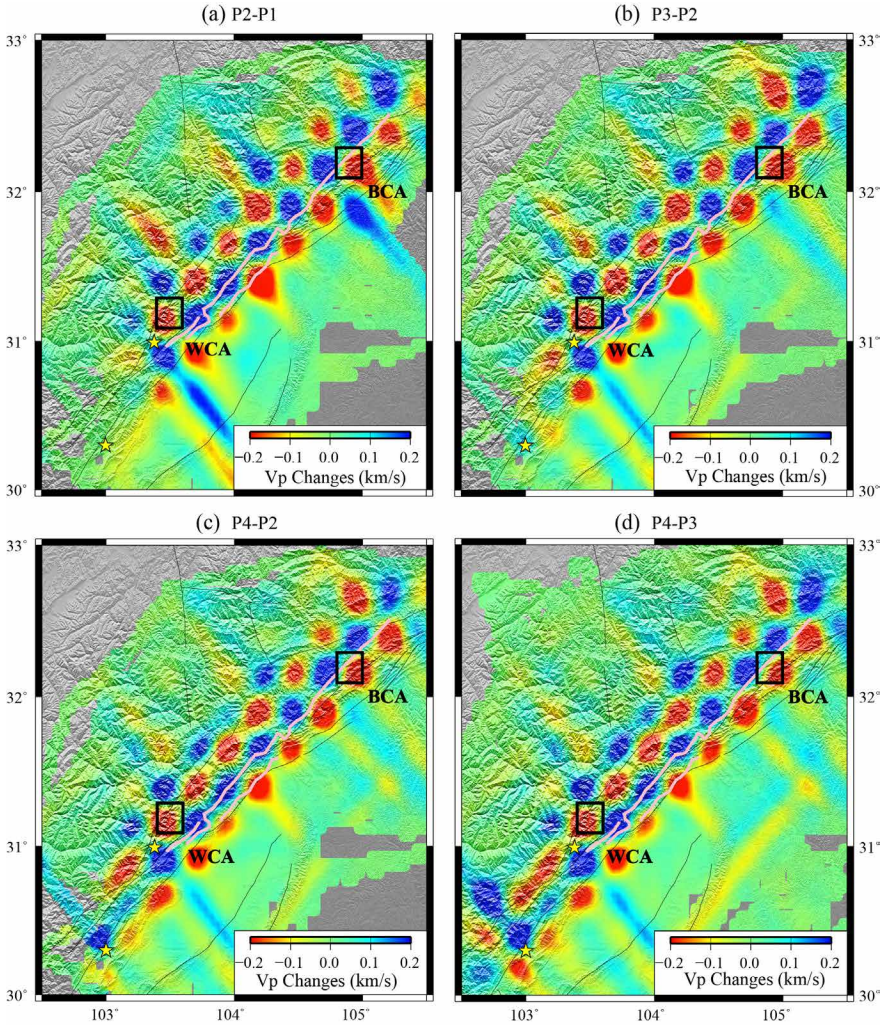

Figure S5. Maps showing the results of 0.25º×0.25º checkerboard tests of the four periods, which indicate that the checkerboard anomalies can be nearly recovered around the Longmenshan fault zone.

We also conducted checkerboard test using a depth dependent 3-D velocity model and 3-D ray tracing to evaluate the lateral resolution of the Pg dataset. More specifically, we chose a 1-D background model consisting of three layers. The top sediment layer is 2 km thick with a P-wave velocity of 4.8 km/s, and the bottom crystalline layer is 15 km thick with a P-wave velocity of 6.0 km/s. There is a 3-km thick transition layer in the middle with a velocity increasing linearly from 4.8 km/s to 6.0 km/s. This 1-D reference model was constructed based on the tomographic studies of Zhao et al. (1997) and Pei et al. (2010). We then added a depth-independent checkerboard pattern of velocity perturbations to the above 1-D background velocity model to create a 3-D velocity model. The grid size and the amplitude of velocity perturbations are 0.25º×0.25º and ±6%, respectively. We employed the pseudo-bending technique (Zhang and Thurber, 2003; Pei et al., 2010) to calculate the 3-D synthetic traveltimes, which are treated as the travel time data of P2. The 1-D traveltimes of the background velocity model are considered as the data of P1. We then inverted the two synthetic datasets similarly to the real data inversion to obtain the changes between P1 and P2. The result is shown in Figure S6a, which clearly shows that velocity anomalies in the WCA and BCA areas can be well resolved. The inverted checkerboard anomalies from the 3-D synthetic traveltime data are very similar to those inverted from 2-D synthetic traveltimes computed with hypothetic straight-line raypaths (Figure S6b). This 3-D test not only suggests that our data have a lateral resolution of 0.25º×0.25º within the Longmenshan fault zone, but also implies that our 2-D method under the assumption of straight-line Pg raypaths is accurate and valid.

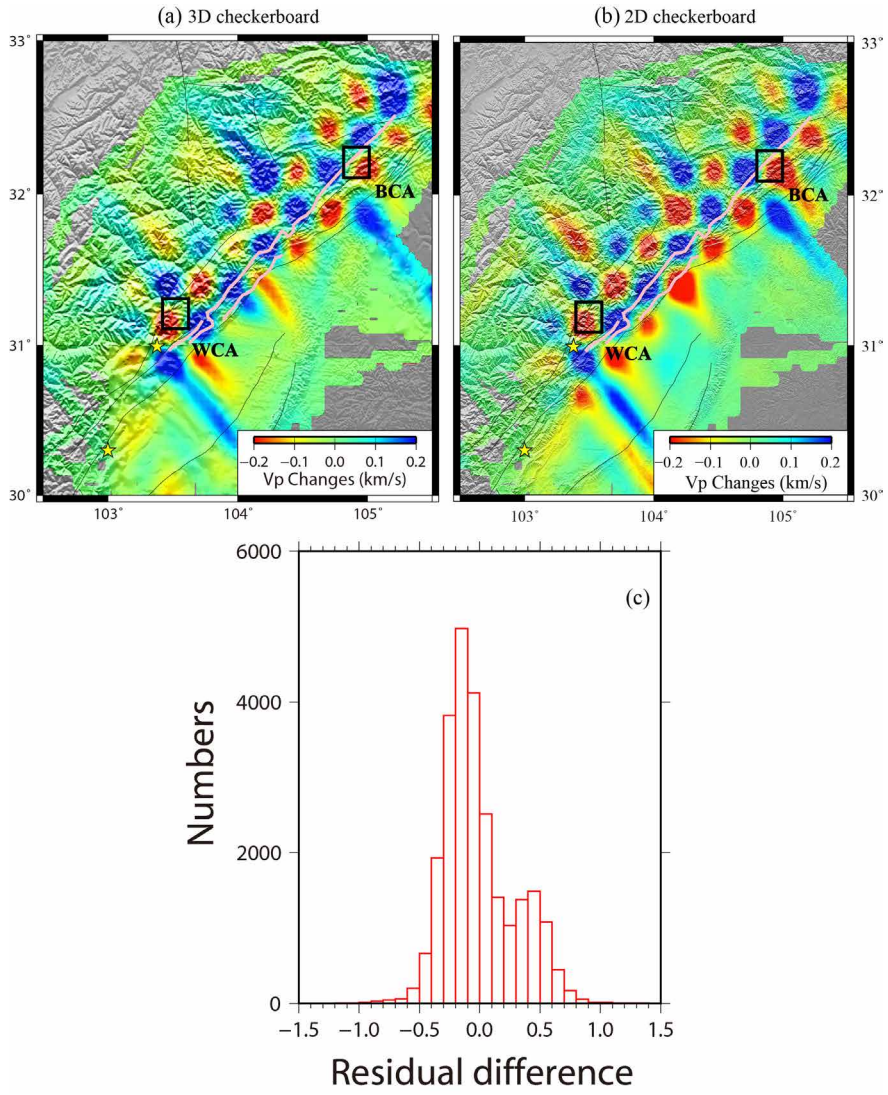

Figure S6. Maps showing the comparison of 0.25º×0.25º checkerboard tests of P2-P1 between the 3-D and 2-D methods. (a) Resolution from a 3-D velocity model using 3-D ray tracing. (b) Resolution from the 2-D method. (c) The histogram of traveltime differences between the 3-D and 2-D method. In general, the travel time differences are insignificant as compared to their residuals, and have a mean of -0.01s and a standard deviation 0.29s.

S4. Robustness tests

We performed a number of tests to evaluate the stability of the inversion results. We first applied a bootstrap technique to estimate the uncertainties in the inverted spatial and temporal velocity variations. We created a new dataset from the original Pg data by using sampling with replacement, and then inverted the data similarly as the real inversion. We repeated this procedure for 100 times, and then computed the standard deviation of all the solutions, which is shown in Figure S7. The maximum variation is less than 0.03 km/s, which is far less than the observed temporal velocity changes observed at the Wenchuan and Beichuan asperities (~0.2 km/s).

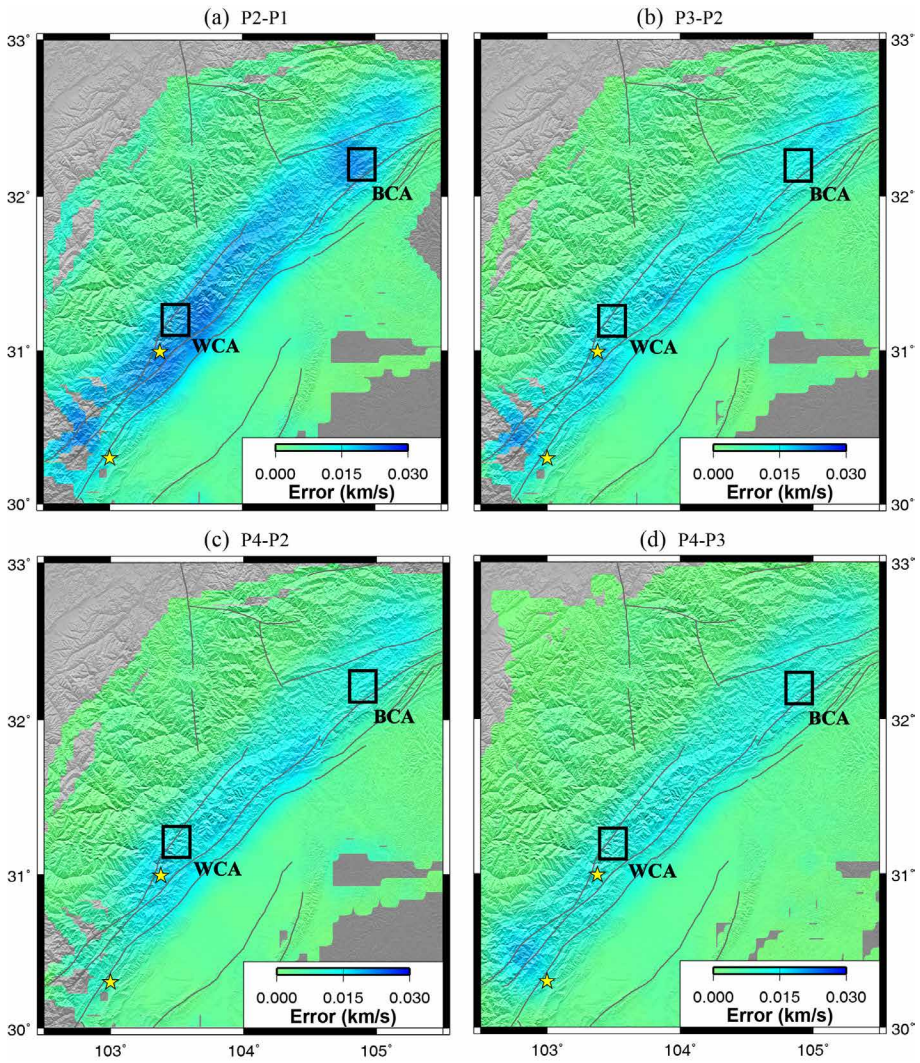

Figure S7. Maps showing the results of the bootstrap variations of the four periods, which indicate the maximum uncertainty to be less than 0.03 km/s. The error is far less than the observed velocity changes at the Wenchuan and Beichuan asperities, which has amplitude around 0.2 km/s.

We further investigated how our results could be affected by data of stations in the two asperity areas. This is done by sequentially removing the traveltime data from stations closest to one of the two asperities before the inversion. The resulting coseismic velocity changes are shown in Figure S8a, and Figure S8b, respectively. The inverted velocity drops at the two asperity areas are still distinct, although their amplitudes are significantly reduced. We also removed data from the newly installed stations after the Wenchuan earthquake and redid the inversion with the same stations across the first and second periods. The inverted velocity changes remain more or less the same (Figure S8c). Figure S8d shows the coseismic velocity changes if we treat all stations in period P1 and P2 as different stations, i.e. using different station terms in these two periods. The fact that the observed velocity changes at the WCA and

BCA are still robustly shown (Figure S8d) even with introducing time-dependent site corrections suggests that the observed data cannot be explained with such time-dependent site corrections

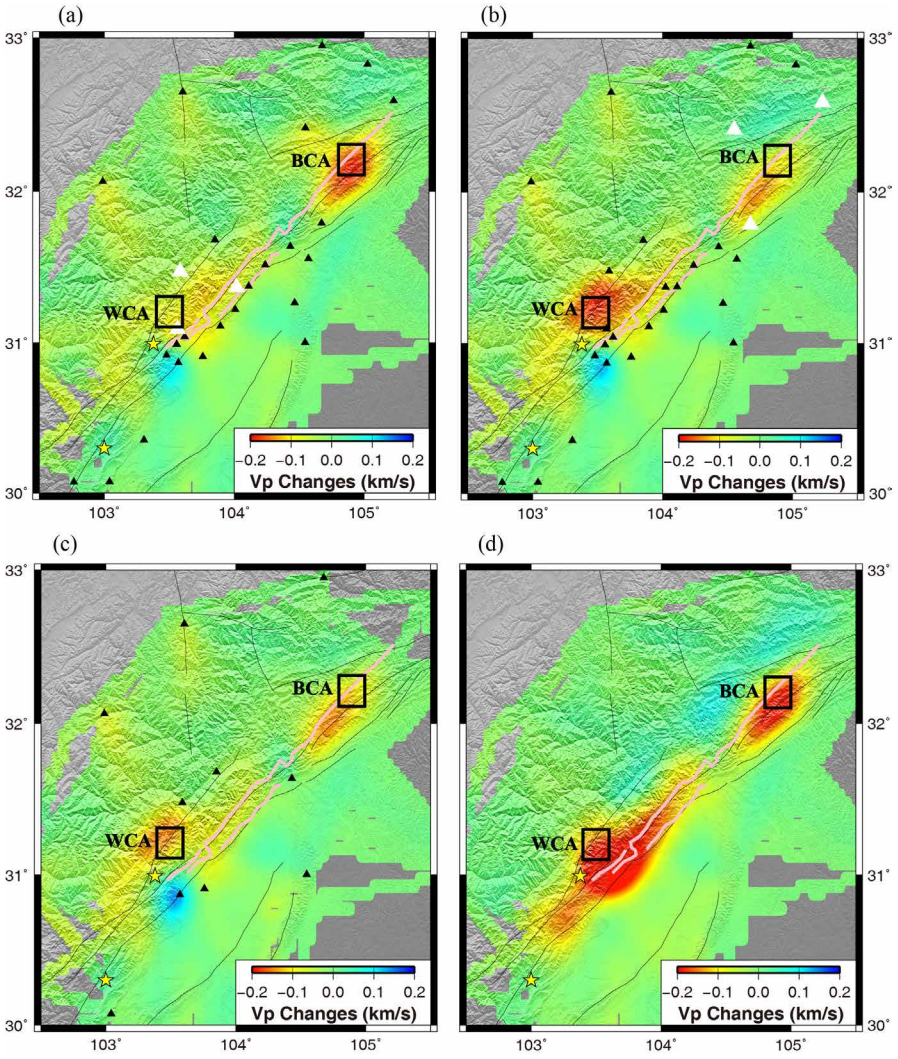

Figure S8. Maps showing the coseismic velocity changes using data from different station sets. (a) removing the data recorded by three stations (white triangles) close to the WCA, (b) removing the data recorded by three stations (white triangles) close to the BCA, (c) Using only same stations (black triangles) in period P1 and P2, (d) Using different station term in period P1 and P2.

We also conducted 3D tomography to verify the 2D inversion. We employed the exactly same data of the 2D inversion to image 3D structure changes before and after the Wenchuan earthquake. The same strategy was adopted in 3D tomography that station terms and event terms were added in the travel time equations to represent very local structure near stations and earthquake depth or origin time errors, and two regularization parameters were used in LSQR for smoothing lateral and vertical variations and damping velocity changes between period P1 and P2. We used the 1D model of the 3D checkerboard test as the initial model, which consists of a 2 km thick top layer and a 15 km thick bottom layer with a constant velocity of 4.8 km/s and 6.0 km/s, respectively, and a 3 km thick middle layer with a velocity

increasing linearly from 4.8 km/s to 6.0 km/s. Finally, the velocity changes in all three layers were obtained by a 3D tomographic inversion. The coseismic velocity changes of the three layers are shown in Figure S9a, S9b and S9c, respectively. The Figure S9d shows the thickness-weighted average velocity changes of three layers. The velocity drops at the two asperity areas, WCA and BCA, are clearly shown in the second and third layers, which have better ray coverage as compared to the first layer. The weighted average velocity changes, which are inherited primarily from those of the third layer due to its large weighting (75%), are almost the same as those derived from the 2D inversion shown in Figure 3a, suggesting that a 2D inversion is suitable to image velocity changes with the type of data and geometry of the study area.

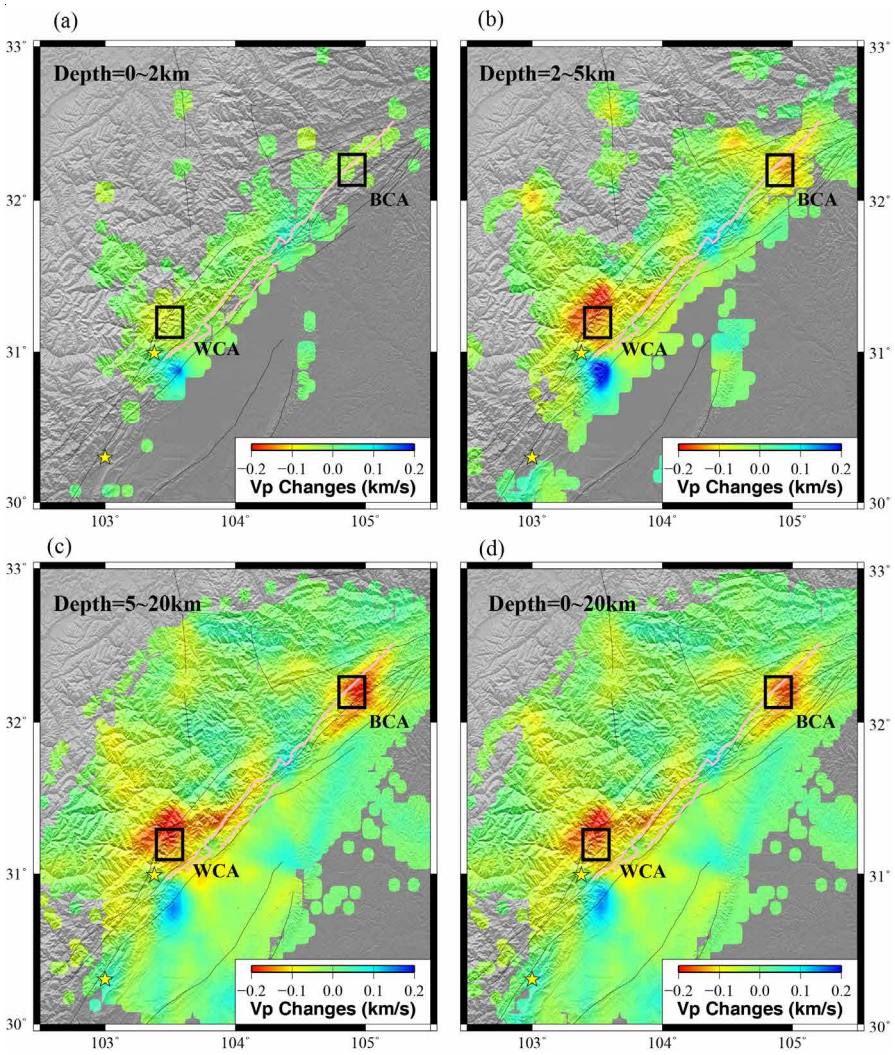

Figure S9. Maps showing the coseismic velocity changes between period P1 and P2 from 3D tomography at different depths: (a) velocity changes at depth of 0~2km, (b) velocity changes at depth of 2~5km, (c) velocity changes at depth of 5~20km. The average velocity changes of the three layers computed by using layer thickness as the weighting factor are shown in (d).

References

Zhao, Z., Fang, J., Zhen, S, Hasegawa, A., Horiuchi, S. Crustal structure and accurate hypocenter determination along the Longmenshan fault zone. *Acta Seismol. Sin*. **6**, 761‑768 (1997) (in Chinese).

Pei, S. et al. Three-dimensional seismic velocity structure across the 2008 Wenchuan Ms8.0 earthquake, Sichuan, China. *Tectonophysics* **491**, 211‑217 (2010).

Zhang, H. & Thurber, C.H. Double-Difference Tomography: The Method and Its Application to the Hayward Fault, California. *B. Seismol. Soc. Am*. **93**, 1875‑1889 (2003)